Available online www.jsaer.com

***Journal of Scientific and Engineering Research*, 2023, 10(8):90-102**

Research Article

ISSN: 2394-2630
CODEN(USA): JSERBR

Application of Fourier Transform for Improved Analysis and Drag Prediction of a Minibus with Open Boot

Olusola Oloruntoba[1*], Adebunmi Okediji[2], Oluwasanmi Alonge[2]

[1]Department of Automotive Engineering, Elizade University, P.M.B. 002, Ilara-Mokin, Ondo State, Nigeria;
[2]Department of Mechanical Engineering, Elizade University, P.M.B. 002, Ilara-Mokin, Ondo State, Nigeria
Email: olusola.oloruntoba@elizadeuniversity.edu.ng

Abstract In a previous study found in literature, the effects of *speed* and *boot-opening* on aerodynamic drag, fuel consumption and CO_2 emission of a typical minibus was studied. The output from the study serve as useful potentials tools for road transport regulatory bodies, such as the Federal Road Safety Corps. The study's developed equations' prediction accuracy of *Total-drag-coefficient* ranges between 0 % and 11.9 % absolute-error. This study's objectives are to: (a) use wavelet analysis to provide detailed operating-regime for regulatory purpose, and (b) apply Fourier Transform for the Analysis and improved prediction of Aerodynamic Drag of a Minibus with Open-Boot. First, Computational Fluid Dynamics is used to predict the aerodynamics for typical minibus. Thereafter, the resulting wavy plots of *Total-drag-coefficient* versus *boot-opening* are combined, for different speed, into a single irregular wave-like plot, using a method developed in this study. Then, wavelet analysis is applied to the single irregular wave-like plot to identify *boot-opening* and *speed* where extremes *Total-drag-coefficient* occur; and gives a detailed operating-regime relevant for regulation. Fourier Transform is then applied to predict *Total-drag-coefficient* for arbitrary *speed* and *boot-opening*. The results obtained show that the occurrence of extremes *Total-drag-coefficient* corresponds with previous study. It further shows additional occurrence of minimum *Total-drag-coefficient* at *boot-opening* 41.56^0. This anomaly with previous study's results is attributed to geometry and/or mesh-influenced turbulent flow. Prediction accuracy improved to maximum absolute-error 0.00841 %.

Keywords Aerodynamic Drag, Open Boot, Prediction, Fourier Transform, Wavelet

1. Introduction

Aerodynamic drag constitutes a major consideration in vehicle performance evaluation and must be critically considered at the Front-End-Engineering-Design (FEED) and Detailed-Engineering-Design (DED). Since aerodynamics drag is majorly affected (and can be controlled) by geometry, various shapes and geometry modifications have been employed to reduce aerodynamic losses [1]–[4]. The determination of aerodynamic drag for vehicles cuts across experimental, empirical and numerical approaches [5]. At the FEED stage, experimental determination of aerodynamic drag is generally not available, while empirical approximations are often limited by inherent error-prone prediction due to potentially different operational conditions from which such empirical prediction models have been developed. DED is also liable to such limitations as FEED. Thus, numerical approximations via Computational Fluid Dynamics (CFD) have been established and adopted as a preferred design tool for the determination of aerodynamics drag. However, numerical approximations of aerodynamics are subject to contending objectives of computational accuracy verses computational speed. As established in published literature [6], [7], finer CFD mesh generally leads to improved prediction accuracy but at a higher demand on computational resources and increased computational time. Thus, empirical approximations are still viable where quick and reasonably accurate aerodynamic drag predictions are required.

In a previous study found in literature, the effects of *speed* and *boot-opening* on aerodynamic drag, fuel consumption and CO2 emission of a typical minibus was studied. [6]. The work resulted in the development of polynomial prediction models to predict aerodynamic drag, fuel consumption and CO_2 emission. The prediction accuracy of the developed polynomial prediction models for estimating *Total drag coefficient* is between 0% and 11.9% of absolute error. The study prediction regression models for *Total drag coefficient* are for vehicle speed at discrete values of $60km/h$, $80km/h$, $100km/h$, $120km/h$, and $140km/h$, and did not capture prediction at other vehicles speeds. Furthermore, a detailed operating regime to relate *Total drag coefficient, vehicle speed, and boot opening*; this would be relevant for road transport regulatory organisations, such as the Federal Road Safety Corps (FRSC). The present study aims to address the identified limitations in the previous study. Thus, the objectives of this study are: (a) to use wavelet analysis to provide detailed operating regime for regulatory purpose, and (b) to apply Fourier Transform for the Analysis and improved prediction of Aerodynamic Drag of a Minibus with Open Boot. Detailed model description, as well as findings, for accomplishing this goal is provided presently.

2. Model Description

This section presents application of Fourier Transform (FT) for the Analysis and Prediction of Aerodynamic Drag of a Minibus with Open Boot. First, a brief description of the problem and solution procedure for the application of Computational Fluid Dynamics (CFD) to obtain total aerodynamic drag for minibus with open boot are provided. Thereafter, Wavelet analysis and the development of prediction model using Fourier Transform are presented.

2.1 Problem Description

The problem description, as given in a previous study [6], outlines CFD analysis of TOYOTA™ HiAce™ (2020 model) minibus as shown in Figure 1(a). A Computer Aided Drawing (CAD) model of a full-scale minibus employed is geometrically given as: overall length L (5.915 m), width W (1.950 m) and height H (1.990 m). Figure 1(b) shows a pictorial illustration of typical TOYOTA™ HiAce™ minibus with open boot, while Figure 2(a) illustrates a geometrically simplified TOYOTA™ HiAce™ minibus with boot opening at $\theta = 5^0$ and $\theta = 90^0$ [6].

(a) TOYOTA™ HiAce™ minibus; 2020 model (Source: Toyota, 2020)

(b) Pictorial illustration of typical TOYOTA™ HiAce™ minibus with open boot.

Figure 1: TOYOTA™ HiAce™ minibus; (Source: [6]).

Figure 2(b) presents the numerical wind tunnel employed; the applicable geometrical dimensions are $14L$ (length), $9W$ (width) and $5H$ (height). These have been adapted, with minor modifications, from the study of Zhang et al. [8] and Ashton & Revell [9]; symbols L, W and H have been previously defined.

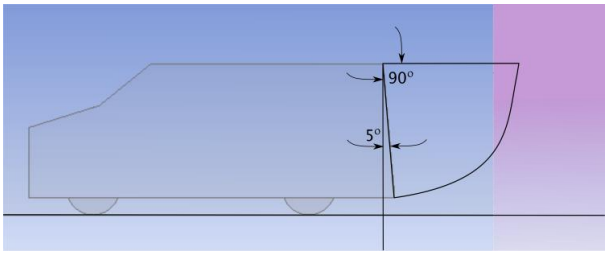

(a) A geometrically simplified TOYOTA™ HiAce™ minibus with boot opening at $\boldsymbol{\theta = 5^0}$ and $\boldsymbol{\theta = 90^0}$.

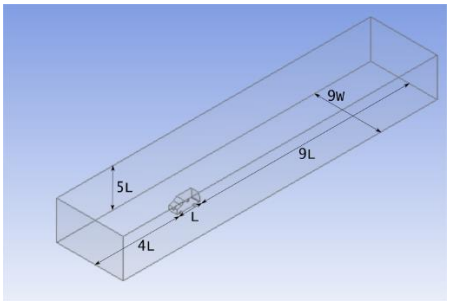

(b) Pictorial illustration of a numerical wind tunnel with a geometrically simplified TOYOTA™ HiAce™ minibus; dimension given in terms of minibus length (L) and width (W).

Figure 2: TOYOTA™ HiAce™ minibus; (Source: [6]).

2.2 Governing equations

The governing equations which describes the aerodynamics air flow around a minibus with open boot includes three equations, namely mass conservation equations (Equation (1)), momentum conservation equations (Equation (2)), and Energy Equation. These are partial differential equations and are also termed as the Navier-Stokes equations (NSE). For the present study, the energy equation is ignored since temperature is not expected to vary significantly. Equations (1) and (2) present the general compressible form of the mass conservation and momentum conservation equations [8], [10]. The symbols $\vec{v}$, ρ, P, $\bar{\bar{\tau}}$ and $\rho\vec{g}$ represent velocity vector of minibus, density of air, static pressure of air medium, stress tensor of air flow and gravitational body force with respect to air flow respectively.

$$\frac{\partial \rho}{\partial t} + \nabla \cdot (\rho \vec{v}) = 0, \quad \textbf{(1)}$$

$$\frac{\partial (\rho \vec{v})}{\partial t} + \nabla \cdot (\rho \vec{v} \vec{v}) = -\nabla P + \nabla \cdot (\bar{\bar{\tau}}) + \rho \vec{g}, \quad \textbf{(2)}$$

Equation (3) presents definition of stress tension for air flow round a minibus, where symbols μ and I represents molecular viscosity and unit tensor respectively. SST $k - \omega$ viscous model is applied for Turbulence modelling [8], [10].

$$\bar{\bar{\tau}} = \mu \left[(\nabla \vec{v} + \nabla \vec{v}^T) - \frac{2}{3} \nabla \cdot \vec{v} \mathrm{I} \right], \quad \textbf{(3)}$$

2.3 Boundary conditions

Applicable boundary conditions are described for the numerical wind tunnel geometrically described in previous section [11], [12]. In order to effectively move minibus motion, air flows into the wind tunnel from the inlet boundary, and against the frontal area of the minibus. This air flow exits the numerical wind tunnel via the exit boundary. Numerical consistency of CFD simulations requires that one of inlet and outlet boundaries be assigned velocity boundary, and the other assigned as pressure boundary. Since forward motion of the minibus is equivalent to air flow velocity against the front of the minibus, the inlet boundary is taken as velocity boundary, and the exit is assigned as the pressure boundary. The ground of the wind tunnel is described as a moving wall, while symmetry planes are applied to the top and side walls.

2.4 Meshing and Simulation

Polyhedral volume mesh is applied in the geometric discretisation of the wind tunnel and vehicle exterior flow domain; since this type of mesh results in finite volumes (FV) coming in contact with several other finite volumes, resulting in better gradient approximations of parameter of interest and accuracy, quick convergence, and low demand on computation resources and time [13]–[15]. Figure (3) illustrates the polyhedral mesh for vehicle speed at $60km/h$ and boot opening at 5^0.

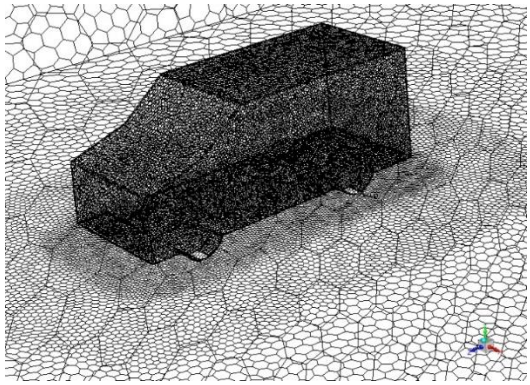

Figure 3: Typical polyhedral mesh for vehicle speed at $\mathbf{60}\boldsymbol{km/h}$ *and boot opening at* $\mathbf{5^0}$*; (Source: [6]).*

A total of 95 simulation cases are studied, and ranges between $60km/h$ and $140km/h$ for inlet velocity at $20km/h$ interval, as well as boot opening between 0^0 and 90^0 at interval of 5^0. The compressible governing equations described earlier are discretised using the finite volume numerical scheme, and solved using ANSYS™ FLUENT™ Density-Based solver. Pressure-velocity coupling is achieved via Implicit solution method. Turbulence modelling is incorporated by the SST $k-\omega$ viscous model. For spatial discretisation in ANSYS™ FLUENT™, the choice of gradient employed is *Least Square Cell Based* while the choice of flow is the *Second Order Upwind* method. *Turbulent Kinetic Energy* and *Specific Dissipation Rate* both employed the *First Order Upwind*.

2.5 Drag coefficient

Drag coefficient is determined using the general vehicle performance model [16]–[18] given in Equation (4), where the symbols F_d, M, C_d, A_F, g, α, and C_r represent vehicle propulsion force, mass of vehicle, aerodynamic drag coefficient, vehicle frontal area, acceleration due to gravity, slope, and wheel rolling resistance respectively. The first and second term in Equation (4) represents vehicle inertia and aerodynamic drag respectively. The third and fourth terms describe *road slope* and *rolling resistance* respectively.

$$F_d = M\dot{v} + \frac{1}{2}\rho C_d A_F v^2 + Mg\sin\alpha + C_r Mg\cos\alpha, \quad \textbf{(4)}$$

The vehicle is assumed to undergo steady-state motion. Therefore, the first term on the Right-Hand-Side (RHS) of Equation (4) (that is *inertia*) is neglected. Furthermore, slope is taken as zero for all 95 cases studied. Consequently, the third and fourth terms on the RHS of Equation (4), which stand for *road slope* and *rolling resistance* respectively, are dropped. Expression to determine drag coefficient is then obtained as shown in Equation (5).

$$C_d = \frac{2F_d}{\rho A_F v^2}, \quad \textbf{(5)}$$

2.6 Wavelet Analysis

Wavelet analysis of *Total drag coefficient* of a minibus versus *boot opening* at different *vehicle speed* is carried out in this section, via the use of a continuous wavelet transform (CWT). The motivation to use wavelet analysis in this study lends from successful application of wavelets in various fields of study, including dynamics systems, economics, and general two-dimensional (2D) and three-dimensional (3D) representation of generic systems. Wavelets are small waves which exits in both time and frequency dimensions, and they enable the extraction frequency information relative to the consistent time domain [19], [20].

A continuous wavelet transform $W(s,\tilde{\tau})$ of any given function $a(t)$ is defined as a convolution of the function with a scaled and translated version of the Morlet wavelet $\psi(t)$ as shown in Equation (6) [21].

$$W(s,\tilde{\tau}) = \int_{-\infty}^{\infty} a(t)\psi_{s,\tilde{\tau}}^{*}(t)dt, \quad \textbf{(6)}$$

The scaled and translated version of the Morlet wavelet is defined as shown in Equation (7). Scaling and translation of the Morlet is accomplished using the s and $\tilde{\tau}$ parameters. Parameter s controls the dilation while

parameter $\tilde{\tau}$ shows the location of the wavelet as a function of variable t. The asterisk in Equations (6 & 7) represents complex conjugate.

$$\psi^*_{s,\tilde{\tau}}(t) = \frac{1}{\sqrt{s}}\psi^*\left(\frac{t-\tilde{\tau}}{s}\right), \quad \textbf{(7)}$$

The Morlet wavelet satisfies the conditions:

$$\int_{-\infty}^{\infty}\psi(t)dt = 0, \text{ and } \int_{-\infty}^{\infty}|\psi(t)|^2 dt < \infty \quad \textbf{(8)}$$

The wavelet power spectrum $P(s,\tilde{\tau})$ of the given function $a(t)$ is described by the squared modulus as shown in Equation (9).

$$P(s,\tilde{\tau}) = |W(s,\tilde{\tau})|^2, \quad \textbf{(9)}$$

In this study, however, discrete data will be applied. Thus, a Continuous Wavelet Transform $W_n(s)$ of any given discrete sequence a_n is defined as a convolution of the sequence with a scaled and translated version of the Morlet wavelet $\psi(t)$ as shown in Equation (10) [20].

$$W_n(s) = \sum_{n'=0}^{N}\left(\frac{\delta\tilde{\tau}}{s}\right)a_{n'}\psi^*\left[\frac{(n-n')\delta\tilde{\tau}}{s}\right], \quad \textbf{(10)}$$

The corresponding wavelet power spectrum $P_n(s)$ of any given discrete sequence a_n is defined in Equation (11).

$$P_n(s) = |W_n(s)|^2, \quad \textbf{(11)}$$

The Morlet wavelet is a plane wave modulated by a Gaussian and described in Equation (12), where ω_0 represents nondimensional frequency and taken as a constant value 6 to ensure admissibility condition is satisfied [22].

$$\psi(\eta) = \pi^{-1/4}e^{i\omega_0\eta}e^{-\eta^2/2}, \quad \textbf{(12)}$$

2.7 Fourier Transform for the Prediction of Total Drag Coefficient

Oloruntoba & Okediji illustrate the variation of *Total drag coefficient* of a minibus versus *boot opening* at different *vehicle speed* (Figure (4)) [6]. *Boot opening* considered in the study ranged between 0^0 and 90^0 inclusive, for vehicle speed at 60 km/h to 140 km/h at 20 km/h interval. The study produced a fourth order polynomial prediction model (refer to Equation 13), averaged for all vehicle speed considered, for calculating *Total drag coefficient* as a function of *boot opening* with $\beta_1 = 6\times10^{-8}$, $\beta_2 = -1\times10^{-5}$, $\beta_3 = 5\times10^{-4}$, $\beta_4 = -6.9\times10^{-3}$, and $\beta_5 = 0.5895$; and $R^2 = 0.8217$.

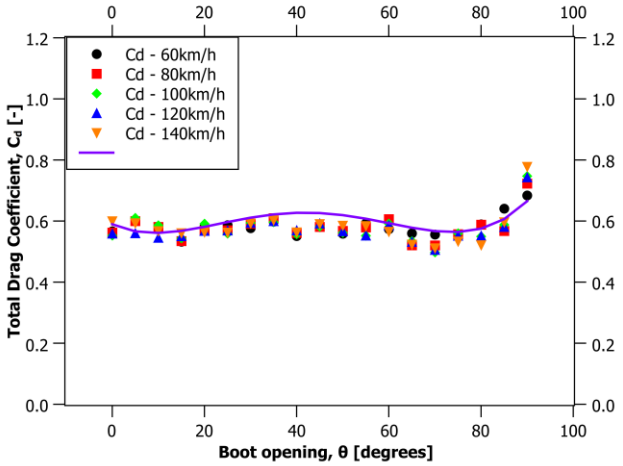

Figure 4: Total drag coefficient of minibus with varying vehicle speeds versus boot opening; (Source: [6]).

$$C_{d,r} = \beta_1\theta^4 + \beta_2\theta^3 + \beta_3\theta^2 + \beta_4\theta + \beta_5, \quad \textbf{(13)}$$

In order to apply Fourier Transform to predict *Total Drag Coefficient* as a function *boot opening* at different *vehicle speed*, Figure (4) is reconstructed in this study to obtain a periodic but irregular wave-like plot as shown in Figure (5). The periodic feature of the reconstructed plot represents *boot opening* range with period of 90^0. There are five cycles which stand for the five *vehicle speed* instances (i.e. 60 km/h, 80 km/h, 100 km/h,

120 km/h and 140 km/h) considered in this study. The irregular feature of the reconstructed plot is due to relatively different values obtained for *Total Drag Coefficient* at these different *vehicle speed* instances.
The mathematical model for reconstructing Figure (4) to obtain Figure (5) is derived by combining Equations (14 & 15) to achieve the final expression shown in Equation (16). Equation (15) represents frequency representation of Discrete Fourier Transform (DFT) of the data given in Figure (5). Equation (14) is derived in this study to transform *boot opening* (range of θ^*: 0^0 – 90^0) at different *vehicle speed* into *periodic representation of boot opening* (range of θ: 0^0 – 470^0). It should be noted that Equations (14 & 16) are only valid for *vehicle speeds* at 60 km/h, 80 km/h, 100 km/h, 120 km/h and 140 km/h.

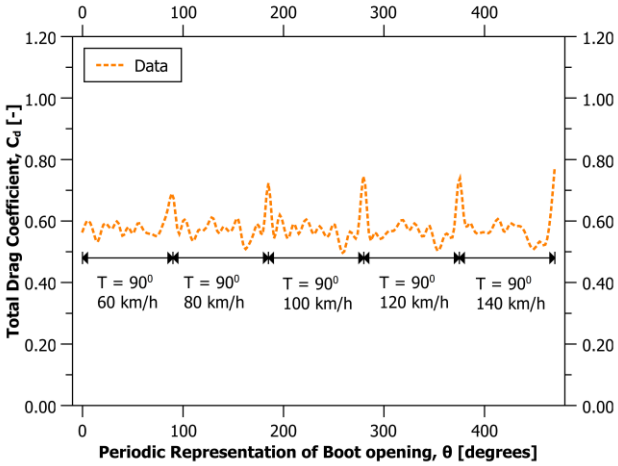

Figure 5: Total drag coefficient of minibus with varying vehicle speeds versus boot opening; (Source: [6]).

$$n = \theta = n(\theta^*, V) = 0.2\theta^* + 0.95(V - 60), \quad \textbf{(14)}$$

The Fourier transform expression for estimating total aerodynamic drag is given in Equation (15):

$$C_{d_n} = \sum_{k=0}^{N-1} M_k \cos\left(\frac{2\pi nk}{N} + A_k\right), \quad \textbf{(15)}$$

Substituting Equation (14) into Equation (15) gives

$$C_d(\theta^*, V) = \sum_{k=0}^{N-1} M_k \cos\left(\frac{2\pi k}{N}\left(0.2\theta^* + 0.95(V - 60)\right) + A_k\right), \quad \textbf{(16)}$$

Where M_k = Magnitude of complex number, A_k = Argument of complex number, N = Number of datapoints. Values of M_i and A_i are given in Table 1 (Appendix A).

2.8 Total aerodynamic drag prediction algorithm for arbitrary vehicle speed and boot opening

The algorithm for the implementation of the Fourier Transform model derived in this study, for the prediction of *Total Drag Coefficient* as a function *boot opening* at different *vehicle speed*, is presented in this section. Figure (6) shows the flowchart for the implementation of *Total Drag Coefficient* prediction algorithm for arbitrary *vehicle speed* and *boot opening*. The algorithm takes *vehicle speed* and *boot opening* as input data, calculates and outputs *periodic representation of boot opening* and *Total Drag Coefficient*.
Since the Fourier Transform model derived in this study, for the prediction of *Total Drag Coefficient* as a function *boot opening* at different *vehicle speed*, is only valid for certain *vehicle speeds* (i.e. at 60 km/h, 80 km/h, 100 km/h, 120 km/h and 140 km/h), approximate solution for arbitrary *vehicle speed* and *boot opening* is given presently. Linear interpolation will be applied to predict *Total Drag Coefficient* at *vehicle speed* other than those used to derive the prediction model, but within the 60 km/h to 140 km/h range. This approximation is expected to give reasonably accurate result, since *Total Drag Coefficient* can be described by a polynomial expression as shown in Equation (13) over the range of *vehicle speed* considered, with a maximum absolute prediction error of 11.9 % [6]. Moreover, prediction via Fourier Transform method proposed in this study is expected to give more accurate prediction than polynomial approach. At *vehicle speed* greater than 140 km/h, threshold *vehicle speed* of 140 km/h is assumed. In a similar approximation, at *vehicle speed* less than 60 km/h,

threshold *vehicle speed* of 60 km/h is assumed. Similar to *vehicle speed*, the developed Fourier Transform model derived in this study to predict *Total Drag Coefficient* is only valid for *boot opening* between 0^0 and 90^0 at 5^0 intervals; linear interpolation can be applied to obtain *Total Drag Coefficient* predictions at other values of *boot opening*.

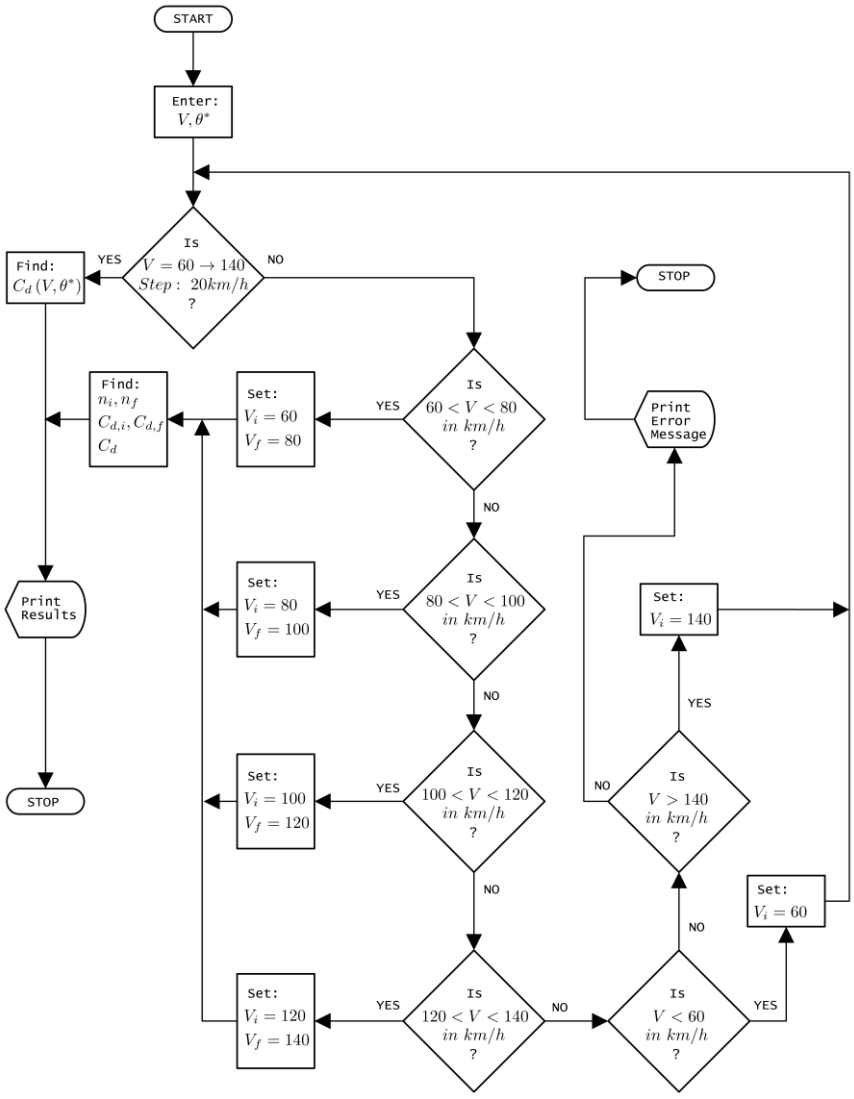

Figure 6: Flowchart for the implementation of total aerodynamic drag prediction algorithm for arbitrary vehicle speed and boot opening

3. Results and Discussion

3.1 Wavelet Analysis

Wavelet power spectra for *Total drag coefficient* of a minibus versus *boot opening* at different *vehicle speed* is presented in Figure (7). The graph shows that the horizontal axis describe *boot opening* series, where a unit represents 5^0 for a total *periodic representation of boot opening* of 470^0; thus, resulting in the horizontal axis having a maximum of 94 index. The vertical axis represents period. It should be noted that the period $T = 90^0$ described in Figure (5) is equivalent to $T_{equi} = 19$ in Figure (7). The corresponding significance of the wavelet power spectra is analysed via a test against the null of AR(1) model. Area of significance in the figure are enveloped by white lines.

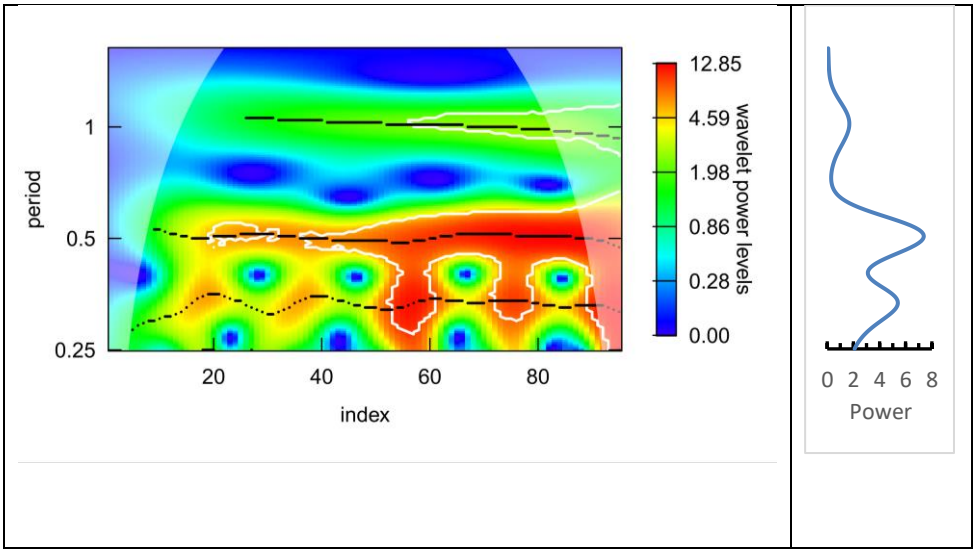

Figure 7: FFT – Wavelet Analysis.

The results in Figure (7) show that *boot opening* at 90^0 has greater impact on *Total drag coefficient* than at other *boot opening* values as indicated by red colour between periods 0.25 and 0.5, especially at *vehicle speed* values of $100\ km/h$, $120\ km/h$ and $140\ km/h$. This can be attributed to two factors, namely: *vehicle speed* and modified vehicle geometry due to *boot opening*. From the theory of aerodynamics, *Total drag coefficient* increases quadratically with *vehicle speed* [23]–[28]; thus, the observed increase in wavelet power with respect to *vehicle speed*. Furthermore, the geometric form of the vehicle due to *boot opening* results in increased vehicle surface for surface friction, and by implication, increased *Total drag coefficient*. Contribution from *pressure drag* to *Total drag coefficient* is negligible as demonstrated in a previous study [6].

In addition, average Reynold's number, Re, and turbulence for the minibus are possible indicator for the observed increased values of *Total drag coefficient*. For air flow round and over the minibus of length, $L = 5.915\ m$, Reynold's number increased linearly from $Re = 6.75 \times 10^6$ at *vehicle speed* $U = 60\ km/h$ to $Re = 1.57 \times 10^7$ at $U = 140\ km/h$. This is an indication of increased turbulent flow characteristics. Although, external flows have been demonstrated in previous studies to be subjective in the estimation of *Total drag coefficient* [29], however, increased *vehicle speed* coupled with favourable vehicle geometry results in increased chaotic turbulent flow and *Total drag coefficient* .

The work of Oloruntoba & Okediji only identified one value for maximum *boot opening* at $\theta^* = 41.84^0$. The authours did not include *boot opening* at $\theta^* = 90^0$ as a maximum value, since *Total drag coefficient* continued to rise at this value of *boot opening*. In this study, however, the introduced period ($T = 90^0$), in Figure (5), for *Periodic representation of boot opening*, θ, results in apparent peaks of *Total drag coefficient* at $\theta = (90^0, 185^0, 280^0, 375^0, 470^0)$, which correspond to peaks for *vehicle speed* $U = (60,80,100,120,140) km/h$ respectively. Consequently, Figure (7) exhibits a ridge (defined as Ridge-1) at period $\tau \cong 1$, which corresponds to $\theta^* = 90^0$ and majorly affects all *vehicle speed* studied with the exception of $U = 60\ km/h$. As described in previous paragraph, vehicle speed as well as coupled effect of modified vehicle geometry due to boot opening and turbulence fluid flow are contributory to this observation. There exist three additional ridges, defined as: Ridge-2, Ridge-3, and Ridge-4. It is apparent that Ridge-2 and Ridge-3 occur at $\tau \cong 0.5$ and $\tau \cong 0.375$ respectively as shown Figure (7), while Ridge-4 is shown in an extended view of Figure (7) as illustrated in Figure (8). Ridge-2 and Ridge-3 correspond to peak values for *Total drag coefficient* at $\theta^* = 42.5^0$ and $\theta^* = 30.63^0$ respectively, and affect all velocity instances studied. Ridge-2 gives a value close to observed value ($\theta^* = 41.84^0$) reported by Oloruntoba & Okediji. At $\theta^* = 41.56^0$, that is between Ridge-2 and Ridge-3, a consistent minimum *Total drag coefficient* occurs for all velocity instances. This is an anomaly from the polynomial model fit presented by Oloruntoba & Okediji for which the authors' prediction of *Total drag coefficient* is approximately close to the maximum value at $\theta^* = 41.84^0$. And the deviation of this observation from the polynomial fit model could be as a result of geometry or mesh influenced turbulent flow. Thus, there is need for more detailed study, via experiments and/or computational fluid dynamics analysis, to capture *Total drag coefficient* trends at finer steps

around this *boot opening* region. Nevertheless, this region of minimum *Total drag coefficient* between Ridge-2 and Ridge-3 is narrow and reflects difficulty in its actual determination. Thus, failure to accurately determine its location would potentially lead to maximum *Total drag coefficient* due to the two bounding ridges. Therefore, the minimum *Total drag coefficient* between Ridge-2 and Ridge-3 should be avoided. Ridge-4 corresponds to peak values for *Total drag coefficient* at $\theta^* = 10.84^0$, compared to the value ($\theta^* = 9.30^0$) observed by [6]; which is a more conservative value for regulation.

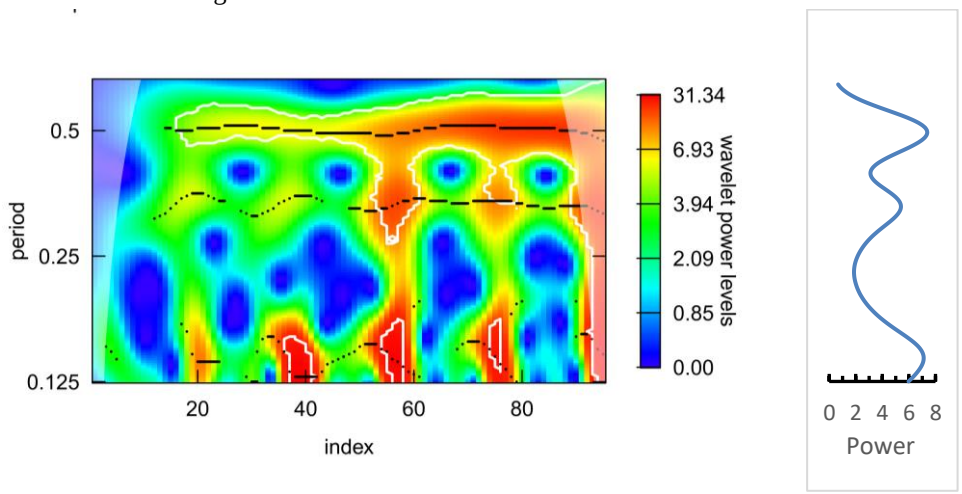

Figure 8: FFT – Wavelet analysis for lower period.

Figure (8) further shows minimum *Total drag coefficient* within two pertinent parts with periods in the vicinity of $0.15625 \leq \tau \leq 0.250$ and $\tau \cong 0.775$ which correspond to *boot opening* of $9.84^0 \leq \theta^* \leq 18.75^0$ and $\theta^* \cong 68.63^0$ respectively. The first part closely matches the range, i.e. $10^0 \leq \theta^* \leq 15^0$, reported in previous studies [6], [30] – [32]. The second part is about 7% lower than the value reported by Oloruntoba & Okediji [6]. Based on the results, *boot opening* at $\theta^* \cong 68.63^0$ exhibits the more consistent minimum *Total drag coefficient* for all *vehicle speed* studied. Apparently, this would be the most preferred choice of *boot opening*. However, there are other factors to be considered. The first consideration is size and weight of load. For large and heavy load to achieve *boot opening* at $\theta^* \cong 68.63^0$ would potentially lead to steady state and transient handling instability and degrade safety. For light and no-load scenarios, the boot could be propped to the desired *boot opening* to achieve the minimum *Total drag coefficient* without major risk to vehicle handling and safety.

The identified ridges exhibit nonlinear wavy pattern which suggests contributions, to each major period, from sinusoids of varying period to reconstruct *Total drag coefficient*. Thus, in order to obtain accurate reconstruction of *Total drag coefficient* profile, all or major sinusoids must be considered. For applications where, noniterative steady state values are required and also with low demand on computational resources, the complete 95 sinusoids presented in Table A-1 are recommended to obtain accurate reconstruction of *Total drag coefficient* profile. But for resource intensive computational applications, selected sinusoids are recommended to achieve a compromise between prediction accuracy and solution speed. The choice of selected sinusoids would also depend on the nature of application.

3.2 Fourier Transform for the Prediction of Total Drag Coefficient

Figure (11) compares the prediction of *Total drag coefficient* using Equation (16) and the numerical data used for developing the prediction model. The vertical axis shows *Total drag coefficient*, C_d, while the horizontal axis shows the *Periodic representation of boot opening*, θ. As described previously, the prediction model expressed as Equation (16) implemented all the 95 sinusoids provided in Table A-1 to achieve accurate prediction of *Total drag coefficient*. Prediction accuracy will be considered presently. Prediction of *Total drag coefficient* for *boot opening* and *vehicle speed* other than the values used in the development of the prediction model will now be considered.

Since a typical minibus' expected *boot opening* can be considered bound between 0^0 and 90^0 inclination, the prediction model described in Equation (16) is expected to give reasonably accurate results. *Boot opening* greater

than 90^0 could lead to prediction error due to inherent limitations in extrapolation and thus the prediction model in this study should not be applied for such scenarios. Furthermore, prediction of *Total drag coefficient* for *boot opening* and *vehicle speed* other than those considered in the development of the prediction model, has been considered via linear interpolation and within the values used for developing the prediction model, as described in the algorithm presented in Figure (6). Thus, excessively high prediction error is not expected. The potential source for major prediction error is in the use of threshold *vehicle speed* when actual *vehicle speed* is greater than $60\ km/h$ or less than $140\ km/h$. Thus, the threshold *vehicle speed* should be applied with caution. Further studies need to be carried out to determine the appropriate parameters for *vehicle speed* outside the bound considered in the development of the prediction model for *Total drag coefficient*.

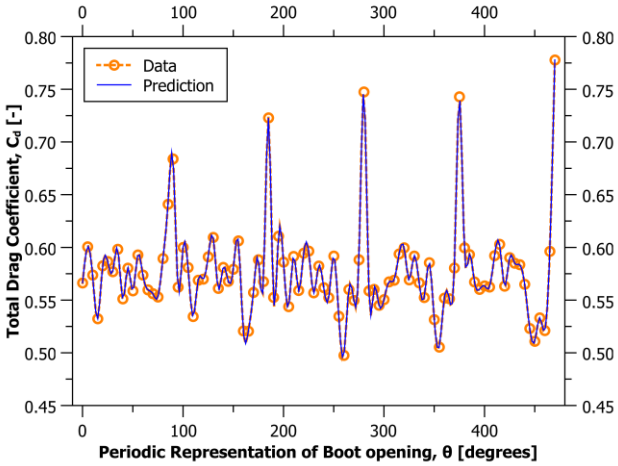

Figure 9: Comparison of total aerodynamic drag prediction with data for minibus' periodically represented boot opening.

Prediction error of Equation (16) in in the determination of *Total drag coefficient* is presented in Figure (10). The vertical axis shows *Prediction Error*, ε, while the horizontal axis represents the *Periodic representation of boot opening*, θ. The result shows that maximum and minimum prediction error are 0.00802% and -0.00841% respectively. The figure further shows that the prediction model is least accurate for *vehicle speed* $60\ km/h$. Although the order of magnitude of prediction error at this *vehicle speed* and other instances of *vehicle speed* are negligible, this occurrence is accounted for by the fact that Equation (16) relied on contributions from all the *vehicle speed* instances considered in the development of the prediction model. And as illustrated in Figure (5), *Total drag coefficient* progressively vary from *vehicle speed* $60\ km/h$ to *vehicle speed* $140\ km/h$, especially at *boot opening* 90^0. Thus, affecting the magnitudes and phases of sinusoids which are shown in Table A-1 and implemented in Equation (16).

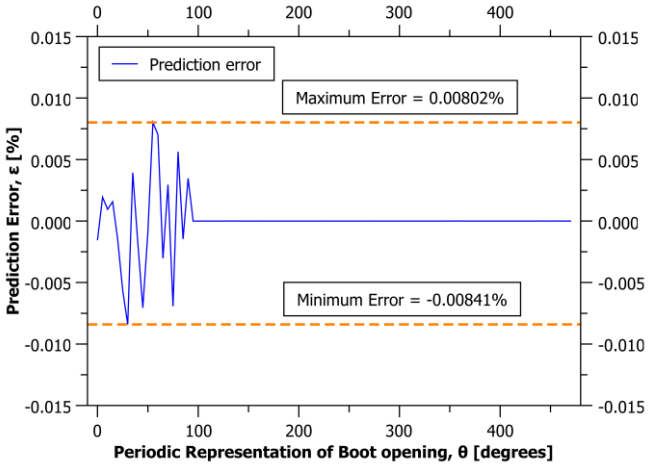

Figure 10: Prediction error plot for total aerodynamic drag prediction of minibus' periodically represented boot opening.

4. Conclusions

The effect of *vehicle speed* and *boot opening* on aerodynamics, fuel consumption and carbon dioxide emission of a typical minibus had been carried out in a previous study. The study resulted in the development of polynomial models for predicting aerodynamic drag, fuel consumption and CO_2 emission. The developed model's prediction accuracy of *Total drag coefficient* was found to range between 0% and 11.9% of absolute error. The objectives of this study are: (a) to use wavelet analysis to provide detailed operating regime for regulatory purpose, and (b) to apply Fourier Transform for the Analysis and improved prediction of Aerodynamic Drag of a Minibus with Open Boot. First, Computational Fluid Dynamics is applied to predict the aerodynamics for typical minibus to obtain wavy plots of *Total drag coefficient* versus *boot opening* at different *vehicle speed*. The resulting wavy plots of *Total drag coefficient* versus *boot opening* at each *vehicle speed* studied are combined into a single irregular wave-like plot, using a method developed in this study. Thereafter, wavelet analysis is applied to the single irregular wave-like plot identify *boot opening* and *vehicle speed* where minimum and maximum *Total drag coefficient* occur; and gives a detailed operating regime relevant for regulatory bodies. This was followed by the application of Fourier Transform to predict *Total drag coefficient* for arbitrary *vehicle speed* and *boot opening*. The results obtained showed that the occurrence of minimum and maximum *Total drag coefficient* corresponded with previous study. This study further showed an additional occurrence of minimum *Total drag coefficient* at *boot opening* 41.56^0 (between Ridge-2 ($\theta^* = 42.5^0$) and Ridge-3 ($\theta^* = 30.63^0$)) which is consistent for all the velocities considered in the study. This anomaly with previous study's results can be attributed to geometry or mesh influenced turbulent flow. Therefore, for regulatory purpose, the minimum *Total drag coefficient* between Ridge-2 and Ridge-3 should be avoided due to uncertainty in prediction using previously developed regression model. Further experimental and/or computational fluid dynamics analysis is required to capture *Total drag coefficient* trends at finer steps around this *boot opening* region. However, prediction accuracy is improved with maximum absolute error of 0.00841%.

Appendix A

Table A-1: Values of Magnitude of complex number (M_k), Argument of complex number (A_k) described in Equation (16).

k	M_k	A_k	k	M_k	A_k	k	M_k	A_k	k	M_k	A_k
0	0.577635	0	24	0.000705	0.479383	48	0.001731	2.510451	72	0.000214	-0.22454
1	0.001964	-0.93896	25	0.00551	1.753976	49	0.001369	1.280161	73	0.002299	-0.54947
2	0.000934	2.863849	26	0.00311	2.587807	50	0.007264	-3.1232	74	0.001871	-2.10037
3	0.001543	-2.30327	27	0.002004	1.953722	51	0.00098	1.444922	75	0.004856	-2.041
4	0.000919	2.918192	28	0.000489	2.962738	52	0.000903	-0.87484	76	0.002985	0.352756
5	0.008326	-0.39367	29	0.002589	-1.49682	53	0.001908	3.11672	77	0.001082	-1.93159
6	0.001947	0.086729	30	0.008121	2.028435	54	0.001493	0.415275	78	0.001513	-0.86225
7	0.002072	-0.29997	31	0.003542	3.116242	55	0.007937	-2.47452	79	0.001383	-1.56624
8	0.002286	-1.82819	32	0.002006	2.612445	56	0.001178	-2.42602	80	0.0136	-1.03336
9	0.002687	-0.83564	33	0.001878	2.256276	57	0.001304	-2.35599	81	0.001274	0.178529
10	0.015943	0.619268	34	0.001598	0.081181	58	0.001825	-3.09117	82	0.001114	-1.79922
11	0.001634	1.230444	35	0.012619	2.872533	59	0.000606	0.930886	83	0.002043	-0.67861
12	0.002043	0.678611	36	0.000606	-0.93089	60	0.012619	-2.87253	84	0.001634	-1.23044
13	0.001114	1.799219	37	0.001825	3.091167	61	0.001598	-0.08118	85	0.015943	-0.61927
14	0.001274	-0.17853	38	0.001304	2.35599	62	0.001878	-2.25628	86	0.002687	0.835636
15	0.0136	1.033364	39	0.001178	2.426018	63	0.002006	-2.61244	87	0.002286	1.828186
16	0.001383	1.566241	40	0.007937	2.474523	64	0.003542	-3.11624	88	0.002072	0.299966
17	0.001513	0.862253	41	0.001493	-0.41528	65	0.008121	-2.02844	89	0.001947	-0.08673
18	0.001082	1.931592	42	0.001908	-3.11672	66	0.002589	1.496821	90	0.008326	0.393666

19	0.002985	-0.35276	43	0.000903	0.874841	67	0.000489	-2.96274	91	0.000919	-2.91819
20	0.004856	2.040998	44	0.00098	-1.44492	68	0.002004	-1.95372	92	0.001543	2.303271
21	0.001871	2.100375	45	0.007264	3.123198	69	0.00311	-2.58781	93	0.000934	-2.86385
22	0.002299	0.54947	46	0.001369	-1.28016	70	0.00551	-1.75398	94	0.001964	0.938964
23	0.000214	0.224541	47	0.001731	-2.51045	71	0.000705	-0.47938			

References

[1]. A. P. Gaylard, N. Oettle, J. Gargoloff, and B. Duncan, "Evaluation of Non-Uniform Upstream Flow Effects on Vehicle Aerodynamics," SAE Int., pp. 692–702, 2014, doi: 10.4271/2014-01-0614.

[2]. T. Schuetz, Aerodynamics of Road Vehicles. Warrendale, Pennsylvania, USA: SAE International, 2016.

[3]. M. I. Mukut and M. Z. Abedin, "Review on Aerodynamic Drag Reduction of Vehicles," Int. J. Eng. Mater. Manuf., vol. 4, no. 1, pp. 1–14, 2019.

[4]. J. Piechna, "A Review of Active Aerodynamic Systems for Road Vehicles," Energies, vol. 14, no. 23, Art. no. 23, Jan. 2021, doi: 10.3390/en14237887.

[5]. W. Zeidan, N. Mazellier, E. Guilmineau, and A. Kourta, "Turbulent wake characteristics of a simplified road vehicle: simulation vs experiment," in Fourth International Conference in Numerical and Experimental Aerodynamics of Road Vehicles and Trains, Aerovehicles4, Berlin, Germany, 2021. Accessed: Apr. 10, 2022. [Online]. Available: https://hal.archives-ouvertes.fr/hal-03365239

[6]. O. A. Oloruntoba and A. P. Okediji, "Effect of Speed and Boot Opening on Aerodynamics, Fuel Consumption, and CO2 Emission of Minibus," FUOYE J. Eng. Technol., vol. 6, no. 4, Art. no. 4, Dec. 2021, doi: 10.46792/fuoyejet.v6i4.665.

[7]. P. C. Sande and S. Ray, "Mesh size effect on CFD simulation of gas-fluidized Geldart A particles," Powder Technol., vol. 264, pp. 43–53, Sep. 2014, doi: 10.1016/j.powtec.2014.05.019.

[8]. C. Zhang, C. P. Bounds, L. Foster, and M. Uddin, "Turbulence Modeling Effects on the CFD Predictions of Flow over a Detailed Full-Scale Sedan Vehicle," Fluids, vol. 4, no. 148, pp. 1–28, 2019, doi: 10.3390/fluids4030148.

[9]. N. Ashton and A. Revell, "Comparison of RANS and DES Methods for the DrivAer Automotive Body Comparison of RANS and DES Methods for the DrivAer Automotive Body," SAE Int., 2015, doi: 10.4271/2015-01-1538.

[10]. ANSYS, ANSYS FLUENT Theory Guide, 17.0. Canonsburg, PA: ANSYS, Inc., 2016.

[11]. H. Chowdhury, R. Islam, M. Hussein, M. Zaid, B. Loganathan, and F. Alam, "Design of an energy efficient car by biomimicry of a boxfish," Energy Procedia, vol. 160, pp. 40–44, Feb. 2019, doi: 10.1016/j.egypro.2019.02.116.

[12]. K. Kurec, M. Remer, T. Mayer, S. Tudruj, and J. Piechna, "Flow control for a car-mounted rear wing," Int. J. Mech. Sci., vol. 152, pp. 384–399, Mar. 2019, doi: 10.1016/j.ijmecsci.2018.12.034.

[13]. M. Sosnowski, J. Krzywanski, and R. Gnatowska, "Polyhedral meshing as an innovative approach to computational domain discretization of a cyclone in a fluidized bed CLC unit," E3S Web Conf., vol. 14, p. 01027, 2017, doi: 10.1051/e3sconf/20171401027.

[14]. M. Sosnowski, J. Krzywanski, K. Grabowska, and R. Gnatowska, "Polyhedral meshing in numerical analysis of conjugate heat transfer," vol. 02096, pp. 4–9, 2018.

[15]. M. L. Thomas and P. W. Longest, "Evaluation of the polyhedral mesh style for predicting aerosol deposition in representative models of the conducting airways," J. Aerosol Sci., vol. 159, p. 105851, Jan. 2022, doi: 10.1016/j.jaerosci.2021.105851.

[16]. S. Borthakur and S. C. Subramanian, "Design and optimization of a modified series hybrid electric vehicle powertrain," Proc. Inst. Mech. Eng. Part J. Automob. Eng., vol. 233, no. 6, pp. 1419–1435, May 2019, doi: 10.1177/0954407018759357.

[17]. I. Darwich, I. Lachhab, and L. Krichen, "Improved Electric Vehicle Performance Using on line PSO approach," in 2019 19th International Conference on Sciences and Techniques of Automatic Control and Computer Engineering (STA), Mar. 2019, pp. 140–144. doi: 10.1109/STA.2019.8717295.

[18]. X. Zhang and C. Mi, Vehicle Power Management: Modelling, Control and Optimization. Springer, 2011. doi: 10.1007/978-0-85729-736-5.
[19]. R. R. Coifman, Y. Meyer, and V. Wickerhauser, "Wavelet Analysis and Signal Processing," in In Wavelets and their Applications, 1992, pp. 153–178.
[20]. C. Torrence and G. P. Compo, "A practical guide to wavelet analysis," Bull. Am. Meteorol. Soc., vol. 79, no. 1, pp. 61–78, 1998.
[21]. B. Cazelles, K. Cazelles, and M. Chavez, "Wavelet analysis in ecology and epidemiology: impact of statistical tests," J. R. Soc. Interface, vol. 11, no. 91, p. 20130585, Feb. 2014, doi: 10.1098/rsif.2013.0585.
[22]. M. Farge and others, "Wavelet transforms and their applications to turbulence," Annu. Rev. Fluid Mech., vol. 24, no. 1, pp. 395–458, 1992.
[23]. Y. Chen and C. R. Müller, "Development of a drag force correlation for assemblies of cubic particles: The effect of solid volume fraction and Reynolds number," Chem. Eng. Sci., vol. 192, pp. 1157–1166, Dec. 2018, doi: 10.1016/j.ces.2018.08.027.
[24]. A. Esteghamatian, F. Euzenat, A. Hammouti, M. Lance, and A. Wachs, "A stochastic formulation for the drag force based on multiscale numerical simulation of fluidized beds," Int. J. Multiph. Flow, vol. 99, pp. 363–382, Feb. 2018, doi: 10.1016/j.ijmultiphaseflow.2017.11.003.
[25]. T. Kubota, H. Ishikawa, and S. Takada, "Drag of a cylindrical object in a two-dimensional granular environment," EPJ Web Conf., vol. 249, p. 03033, 2021, doi: 10.1051/epjconf/202124903033.
[26]. M. Maza, K. Adler, D. Ramos, A. M. Garcia, and H. Nepf, "Velocity and Drag Evolution From the Leading Edge of a Model Mangrove Forest," J. Geophys. Res. Oceans, vol. 122, no. 11, pp. 9144–9159, 2017, doi: 10.1002/2017JC012945.
[27]. S. Takada and H. Hayakawa, "Drag Law of Two-Dimensional Granular Fluids," J. Eng. Mech., vol. 143, no. 1, p. C4016004, Jan. 2017, doi: 10.1061/(ASCE)EM.1943-7889.0001054.
[28]. J. Y. L. Tay, G. Zotz, J. Puczylowski, and H. J. R. Einzmann, "Go with the flow: The extent of drag reduction as epiphytic bromeliads reorient in wind," PLOS ONE, vol. 16, no. 6, p. e0252790, Jun. 2021, doi: 10.1371/journal.pone.0252790.
[29]. G. Tagliavini, M. McCorquodale, C. Westbrook, P. Corso, Q. Krol, and M. Holzner, "Drag coefficient prediction of complex-shaped snow particles falling in air beyond the Stokes regime," Int. J. Multiph. Flow, vol. 140, p. 103652, Jul. 2021, doi: 10.1016/j.ijmultiphaseflow.2021.103652.
[30]. A. Huminic and G. Huminic, "Aerodynamic Study of a Generic Car Model with Wheels and Underbody Diffuser," Int. J. Automot. Technol., vol. 18, no. 3, pp. 397–404, 2017, doi: 10.1007/s12239.
[31]. S. Ahmed, G. Ramm, and G. Faltin, "Some salient features of the time-averaged ground vehicle wake," SAE, vol. Paper No. 840300, 1984.
[32]. R. Strachan, K. Knowles, and N. Lawson, "The vortex structure behind an Ahmed reference model in the presence of a moving ground plane," J Exp. Fluids, vol. 42, no. 5, p. 659−669, 2007.